applied optics

Analyzing colors and spectra of natural rainbows with hyperspectral imaging

Raymond L. Lee, Jr.

Mathematics and Science Division, United States Naval Academy, Annapolis, Maryland 21402, USA (ProfRayLee@gmail.com)

Received 8 January 2020; revised 26 April 2020; accepted 1 May 2020; posted 1 May 2020 (Doc. ID 387757); published 12 June 2020

Few colorimetric analyses of natural rainbows (*i.e.*, bows seen in rain showers) have been published, and these are limited either to approximate techniques (colorimetrically calibrated red–green–blue (RGB) cameras) or to rainbow proxies (bows seen in sunlit water-drop sprays). Furthermore, no research papers provide angularly detailed spectra of natural rainbows in the visible and near-IR. Thus some uncertainty exists about whether the published spectra and colors differ perceptibly from those in natural rainbows. However, battery-powered imaging spectrometers now make possible direct field measurements of the observed chromaticities and spectra in such bows. These data (1) show consistent spectral and colorimetric patterns along rainbow radii and (2) let one subtract additively mixed background light to reveal the intrinsic colors and spectra produced by rainbow scattering in nature.

https://doi.org/10.1364/AO.387757

1. INTRODUCTION

Within atmospheric optics, measuring the colors and visible-wavelength spectra of slowly changing features such as the clear daytime sky has long been possible [1–3]. However, acquiring colorimetric and spectral data from rapidly changing or ephemeral phenomena (*e.g.*, twilight or rainbows) poses an entirely different set of problems: any significant increase in this data's angular, spectral, or temporal resolution usually requires new techniques or instruments. For example, an imaging spectrometer tethered to a laptop computer and external power supply are adequate for measuring skylight spectra during civil twilights [4,5]. Yet the time needed to set up this equipment often makes it inadequate for acquiring the spectra and colors of natural rainbows (*i.e.*, rainbows seen in naturally occurring rain), some of which last for only 5–10 min.

To meet or avoid these time constraints, earlier measurements of natural rainbow colors have relied on (1) approximate techniques such as colorimetrically calibrated red–green–blue (RGB) data from film or digital cameras [4,6,7] or (2) spectra of rainbow proxies such as long-lived spraybows seen in sunlit water-drop sprays [4,8]. Clearly neither approach yields data on natural rainbows measured *in situ* at high spectral and angular resolutions. To get such data consistently during many rainbows' peak-luminance period of just a few minutes requires an imaging spectrometer that is self-contained (*i.e.*, no laptop or external power supply required), quick to set up, highly portable, and able to capture hyperspectral datacubes within seconds.

2. ACQUIRING HYPERSPECTRAL IMAGES OF NATURAL RAINBOWS

One instrument that meets all of these requirements is the Specim IQ hyperspectral camera [9]. This imaging spectrometer is a pushbroom scanner that is configured as a battery-powered, self-contained camera: its internal diffraction grating rotates to produce hyperspectral datacubes with a spatial size of 512-by-512 pixels. The camera's square field of view is $\sim 30°$ or $\sim 0.059°$/pixel in each spatial direction. At each pixel, the camera is spectrally calibrated to measure absolute spectral radiances L_λ for wavelengths λ from $\sim 400 - 1000$ nm in slowly increasing spectral steps of $\Delta\lambda \sim 3$ nm, at a spectral resolution of 7 nm, and at a radiance resolution of 12 bits/$\Delta\lambda$. At typical outdoor lighting levels for low-sun rainbows (horizontal illuminances $\sim 2000 - 2400$ lux under broken clouds), the Specim IQ can acquire a natural rainbow datacube in $\sim 3 - 5$ s.

Figure 1 shows RGB images of a natural rainbow that are calculated [10] from Specim IQ hyperspectral scans at a rural site near Maryland's Chesapeake Bay (see Table 1 for details).

Table 1 parameters include unrefracted sun elevation h_0, rainbow radius r, clock angle α, and normalized colorimetric gamut $\hat{g}$ (see Section 3 for further details).

My inclusion of utility lines, a pole, and trees in Fig. 1 is intentional: these unphotogenic objects provide targets for checking the focus of sky and rainbow images that otherwise lack high-contrast edges. Another inelegant but useful feature is the irregular black "U" shape added to Fig. 1(b)'s lower right: such black masking lets me exclude from analysis any pixels of background objects that adjoin the rainbow. In Fig. 1 and later

Fig. 1. RGB images of a natural rainbow's (a) left and (b) right sides as calculated from hyperspectral datacubes acquired on 14 August 2018 near Owings, Maryland at 1936 EDT (scan6 at unrefracted sun elevation $h_0 = 3.9°$) and 1928 EDT (scan2 at $h_0 = 5.4°$), respectively. The acronym "EDT" means U. S. Eastern Daylight Time (EDT = UTC − 4 h).

Table 1. Chromaticity Parameters for Rainbow Hyperspectral Scans

Figures	Scan Name (Optional)	Location	Date (Month-Day-Year)	h_0 (°)	r Interval (°)	α Interval (°)	Observed Gamut $\hat{g}$	Intrinsic Gamut $\hat{g}$
Figs. 1(a), 2–4	scan6	Owings, MD	8-14-2018	3.9	40.0-43.0	128.9–142.0	0.007138	0.04610
Figs. 1(b), 2–5	scan2	Owings, MD	8-14-2018	5.4	40.0-43.0	37.6–73.2	0.01242	0.05701
Fig. 5		Owings, MD	1-11-2016	9.8	41.1–43.8	1.0–21.6	0.035635	
Figs. 6–9		Marion Center, PA	8-8-2018	1.9	40.0-43.0	35.9–68.0	0.008615	0.05180
Figs. 10(a), 11, 12	scan12	Owings, MD	9-18-2018	12.2	40.2–43.2	148.7–152.7	0.04894	0.1306
Fig. 10(b)		North Beach, MD	9-18-2018	8.5	40.0–43.0	147.0–152.0	0.04993	0.1120

RGB images, the hyperspectral pixels to be analyzed lie within the green borders.

Although the two sides of the same rainbow in Fig. 1 were scanned only a few minutes apart and under the same rainfall conditions, they look markedly different. This visible difference was caused by a bluer and *proportionally* brighter background in Fig. 1(a) than in Fig. 1(b). The latter condition means that the ratio of background cloud luminance L_v to peak observed rainbow L_v is larger in Fig. 1(a). As a result, its rainbow has lower contrast and purity than Fig. 1(b)'s rainbow despite the fact that its peak rainbow L_v is ∼17% greater. To help distinguish between some hyperspectral scans, hereinafter I may use a given day's scan numbers as labels: "scan6" indicates Fig. 1(a)'s left-side rainbow whereas "scan2" indicates Fig. 1(b)'s right-side rainbow.

3. COLORIMETRIC ANALYSIS OF NATURAL RAINBOWS FROM HYPERSPECTRAL IMAGES

Figure 2 shows the colorimetric consequences of these two scans' very different, but spatially adjacent, lighting regimes. In it, we see a segment of the Planckian locus (dashed line) in the CIE 1976 *uniform-chromaticity-scale* (or UCS) diagram, with color-temperature labels identifying this segment's redder and bluer ends. Although the UCS color space itself is nearly perceptually isotropic, the ordinate and abscissa scales differ in Fig. 2 and subsequent chromaticity diagrams in order to show as much colorimetric detail as possible. To give a sense of perceptual scale in this small region of the UCS diagram, near $u' = 0.195$ a local MacAdam color-matching ellipse is plotted in black. Its semiaxes span one *just-noticeable difference* (or JND) for a typical observer [11].

A useful way of organizing Fig. 2's data is to connect each rainbow scan's u', v' coordinates into continuous chromaticity curves that are functions of primary *rainbow radius* r (*i.e.*, angle from the antisolar point). Each of Fig. 2's three chromaticity curves consists of 61 u', v' pairs that span $40° \le r \le 43°$ in steps of $\Delta r = 0.05°$, and each $u'v'(r)$ pair plotted in Fig. 2 and later UCS diagrams is averaged over an interval of *rainbow clock* (or azimuth) *angles* α. In this paper, α follows the trigonometric convention of increasing counterclockwise from 0° at the rainbow's right-hand vertical side, to 90° at its top (*i.e.*, the 12 o'clock position), and to 180° at its left-hand vertical side.

This r, α polar coordinate system has its origin at the antisolar point and does not depend on sun elevation h_0 or on the visibility of any part of the rainbow arc [12]. Only when refracted $h_0 = 0°$ and the horizon is level can the rainbow exist at $\alpha = 0°$ or 180° (different α limits exist at $h_0 = 0°$ if parts of the bow are visible below the local tangent plane). For any hyperspectral scan, the averaging interval $\Delta\alpha$ depends on how much of the

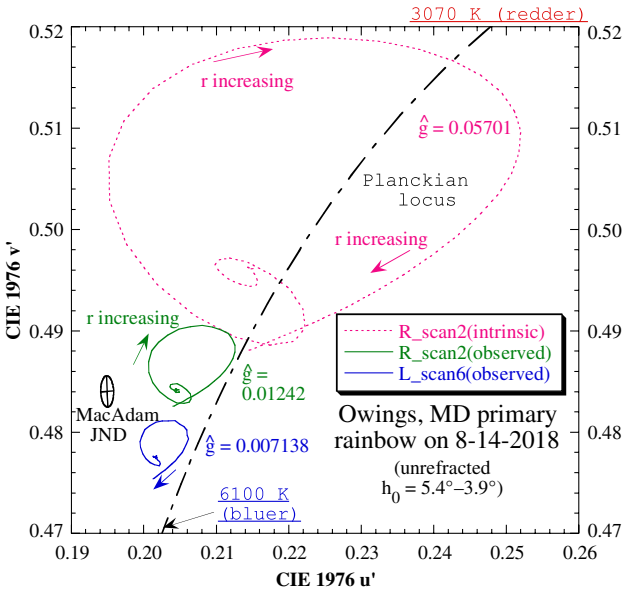

Fig. 2. Portion of the CIE 1976 UCS diagram with chromaticity curves for Fig. 1's observed and intrinsic rainbows as functions of rainbow radius r for $40° \le r \le 43°$. At each r, the mean $u'v'(r)$ are averaged over clock angles $\alpha = 128.9° - 142.0°$ [left-side scan6 or Fig. 1(a)] or $\alpha = 37.6° - 73.2°$ [right-side scan2 or Fig. 1(b)].

rainbow arc is both visible and visually uniform: in Fig. 1, the $\Delta\alpha$ intervals range from 13.1° for scan6 to 35.6° for scan2, or at least 80–205 hyperspectral pixels at each r depending on r and $\Delta\alpha$.

Bearing these geometric details in mind, note that we further distinguish between *observed* rainbows that include background radiances and *intrinsic* rainbows that exclude or subtract these radiances [6]. A convenient technique for calculating intrinsic rainbow chromaticities and spectra is to subtract from the observed rainbow spectra a mean cloud or sky background spectrum for *Alexander's dark band* (ADB) between the primary and secondary bows [13]. To good approximation, the background and intrinsic rainbow spectra are mixed additively. Thus by averaging over a suitably uniform r, α arc within ADB, one can calculate entirely positive rainbow spectra for the intrinsic primary and secondary bows. Each of these intrinsic spectra is a convolution of the sunlight illuminant and the rainbow scattering function in a particular direction.

Figure 2 plots not only Fig. 1's observed $u'v'(r)$ chromaticity curves for scan6 and scan2 but also an intrinsic chromaticity curve for the higher contrast rainbow in scan2 [*i.e.*, Fig. 1(b)]. Because imaging spectrometers provide repeatable, spectrally calibrated u', v' values at all pixels, we can now compare with confidence rainbows' *absolute* chromaticities within the UCS diagram. Several such colorimetric features are striking in Fig. 2.

First, $u'v'(r)$ curves for different segments of the same rainbow need not overlap. In fact, Fig. 2's scan2 and scan6 observed chromaticity curves are separated by a gap of nearly 1 JND, which quantitatively confirms our qualitative impression that Fig. 1's two observed rainbows are visibly different. Second, the scan6 rainbow is discernibly bluer than the scan2 rainbow, meaning that it has visibly higher *correlated color temperatures* or CCTs [14]. This too makes sense, given the bluer and proportionally brighter cloud background in scan6 [*i.e.*, Fig. 1(a)] that produces its less saturated rainbow colors. Third, comparing *normalized colorimetric gamuts* $\hat{g}$ [15] for scan6 and scan2 confirms that the former's observed rainbow colors are visibly less saturated (*i.e.*, its chromaticity curve spans a smaller area on the UCS diagram). In fact, the ratio of observed $\hat{g}$ (scan2)/$\hat{g}$ (scan6) ~1.74, or scan2 in Fig. 1(b) is markedly more saturated. Fourth, the $\hat{g}$ ratio for scan2's intrinsic and observed rainbows is larger at ~4.59 (see Table 1 for details). Not surprisingly, subtracting the bluish mean ADB spectrum not only greatly expands the rainbow's color gamut but also reddens it by shifting all of its $u'v'(r)$ to lower CCTs.

Figure 3 shows the results of applying the same kind of intrinsic filtering to both of Fig. 1's two rainbow segments. In Fig. 3 and subsequent UCS diagrams, blue and red labels indicate the CCT extremes of the plotted Planckian locus. When the scan2 and scan6 observed rainbow spectra have their corresponding mean ADB spectrum subtracted, the resulting intrinsic rainbow spectra yield $u'v'(r)$ chromaticity curves that are much more similar: in Fig. 3, the two curves' mean u', v' nearly coincide, and their intrinsic ratio of $\hat{g}$ (scan2)/$\hat{g}$ (scan6) is closer to unity at ~1.24. These changes suggest that removing the two rainbow segments' cloud backgrounds does indeed reveal similar scattering results from their similar raindrop size distributions.

To give a direct visual sense of the differences between observed and intrinsic rainbows, Fig. 4 draws color maps that are calculated from the $u'v'(r)$ chromaticity curves in Figs. 2 and 3. As described in Ref. [10], these color maps are a diligent, but not infallible, attempt to convey an observed rainbow's visual appearance in nature, and here each is paired with its intrinsic counterpart. For legibility, each of Fig. 4's color bars is normalized by a different maximum luminance.

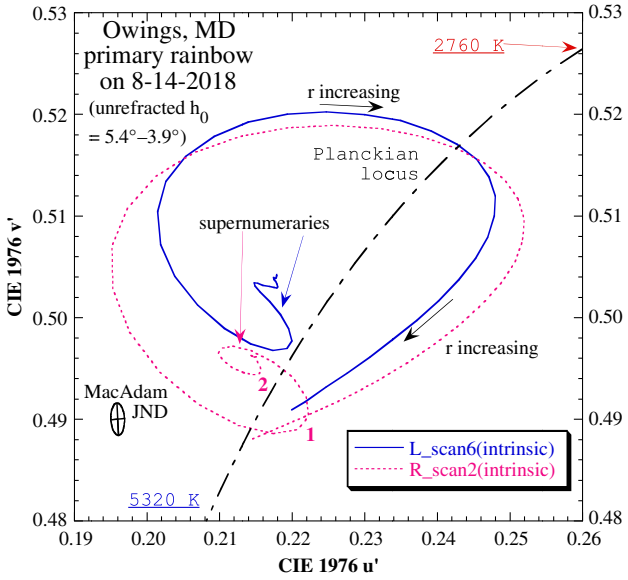

Fig. 3. CIE 1976 UCS diagram with radial chromaticity curves for Fig. 1's intrinsic natural rainbows (scan2 and scan6). The spiral traces at smaller r are characteristic signatures of primary rainbow supernumeraries, with the sharp turns labeled **1** and **2** corresponding to the purplish bands of the first and second supernumeraries.

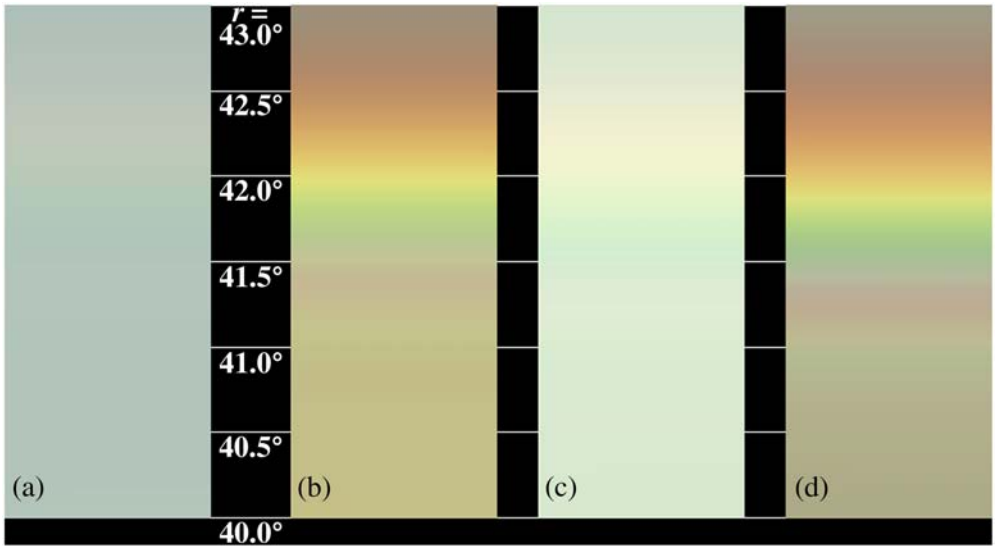

Fig. 4. RGB color bars that are calculated [10] from the $u'v'(r)$ chromaticity curves in Figs. 2 and 3. Here (a) and (b), respectively, plot the observed and intrinsic rainbow colors for scan6 [Fig. 1(a)], whereas (c) and (d) plot those for scan2 [Fig. 1(b)].

Figures 4(a) and 4(c) show the subtle purity increases in observed rainbow colors that result when we shift from scan6 to scan2, respectively (see Fig. 2). In Figs. 4(b) and 4(d), the intrinsic colors for scan6 and scan2 are now mapped directly as opposed to graphically in Fig. 3. In particular, the visually subthreshold observed supernumeraries of Figs. 4(a) and 4(c) become plainly visible in their intrinsic counterparts Figs. 4(b) and 4(d). Compared with the bows' small angular widths in Figs. 1(a) and 1(b), the larger subtense of Figs. 4(a) and 4(c) may make their color bars appear slightly more vivid than in the natural archetypes.

Figure 5 compares the chromaticities of scan2's observed, but fairly bright, natural rainbow with those observed in a spraybow [4]. Both hyperspectral scans share similar features such as their (1) $u'v'(r)$ curves that follow clockwise paths as r increases and (2) hook-shaped or spiral traces that define the primary bow's supernumeraries at smaller r. In Fig. 5 and later figures, some $u'v'(r)$ curves include line markers solely as a way to help identify them.

Yet differences between this spraybow and the natural rainbow are also obvious. The spraybow was scanned at a larger unrefracted h_0 of 9.7°, which typically produces a less-reddened rainbow illuminant. However, clearly the spraybow is redder (*i.e.*, its CCTs are smaller) than Fig. 5's observed rainbow. In addition, $\hat{g}$ for the observed spraybow's colors is nearly 3 times that for the rainbow, even though visually their gamuts seemed comparable. These minor puzzles are partly explained by the matte black background against which the spraybow was measured. First, with no admixture of light from a cloud background, the spraybow lacks the corresponding bluish color bias of the observed natural rainbow. Second, the spraybow's black background also greatly reduces the difference between its intrinsic and observed colors. In fact, subtracting scan2's cloud background yields an intrinsic $\hat{g}$ for the natural rainbow ~1.6 times greater than $\hat{g}$ for the observed spraybow.

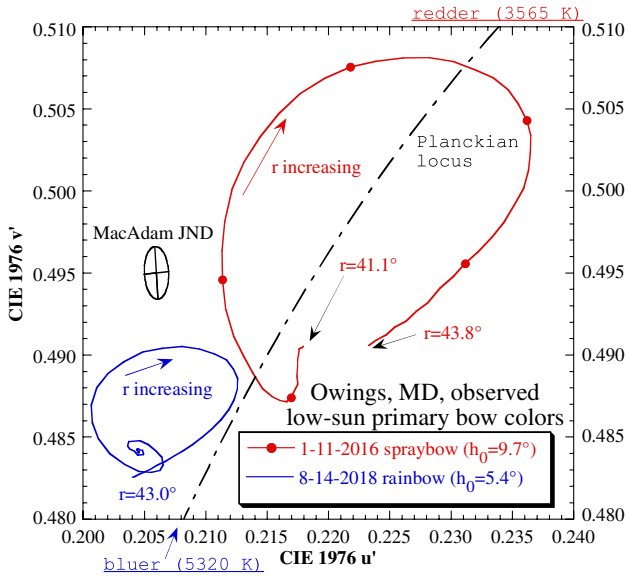

Fig. 5. CIE 1976 UCS diagram with curves of observed natural rainbow (scan2 in Fig. 2) and spraybow chromaticities at low sun elevations. The black background used with the spraybow [4] makes its color gamut larger than that of the natural rainbow; no intrinsic spraybow measurements were possible on 1-11-2016.

4. ADDING SPECTRAL AND PHOTOMETRIC ANALYSES OF NATURAL RAINBOWS

Figure 6 maps both the visible-wavelength (VIS; 400–700 nm) and false near-IR colors (NIR; 700–1000 nm) of a rainbow observed at a rural site in western Pennsylvania (see Table 1 for details). The false-color NIR map is calculated by spectrally shifting each of the CIE color-matching functions upward by 300 nm and then calculating simulated u', v' chromaticities from each hyperspectral pixel's NIR spectrum. One of Fig. 6(b)'s subtlest features is a low-contrast segment of a NIR secondary rainbow just visible in its upper right.

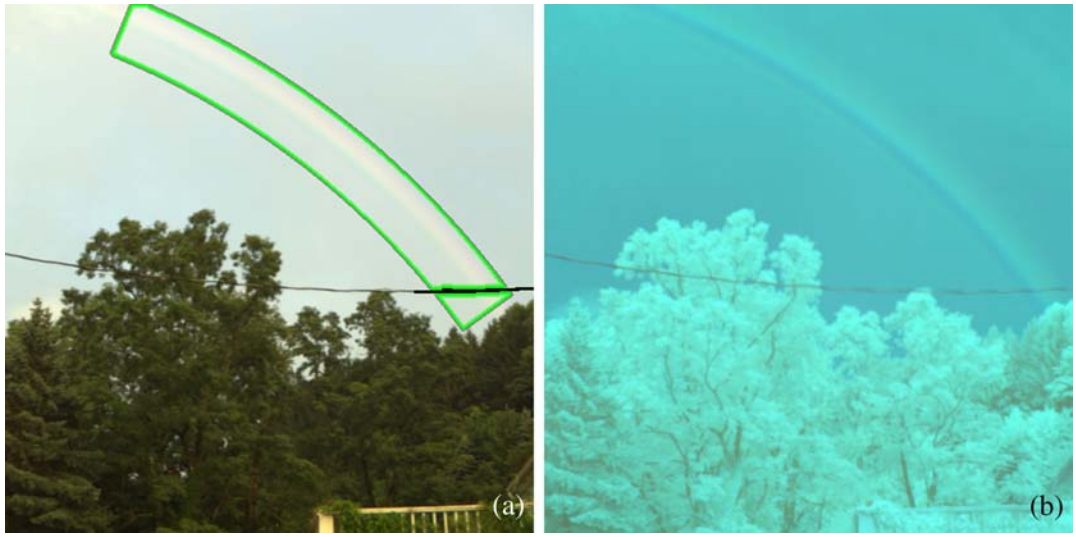

Fig. 6. RGB images of a natural rainbow's observed (a) visible-wavelength (VIS) and (b) false near-IR (NIR) colors calculated from a hyperspectral datacube acquired on 8 August 2018 near Marion Center, Pennsylvania at 2008 EDT when the unrefracted $h_0 = 1.9°$. The hyperspectral pixels to be analyzed in Fig. 6(a) lie within the green border.

Because liquid water's index of refraction n slowly decreases with increasing λ in both the visible and NIR [16], minimum deviation angles are smaller for NIR primary rainbows. As a result, these NIR rainbows [17,18] occur at slightly larger r than their VIS counterparts, and my calculations for Fig. 6 estimate that its NIR and VIS rainbows' outer edges are separated by $\Delta r \sim 0.7°$. Given the wavelength and visual uncertainties of locating a minimum deviation radius in these low-contrast rainbow images, this estimate agrees reasonably well with $\Delta r \sim 0.32°$ for primary radii calculated as functions of $n(\lambda)$ at $\lambda = 682$ nm and 899 nm. Alternatively, using two monochromatic images from Fig. 6's hyperspectral data at $\lambda = 682$ nm and 899 nm yields an improved estimate of the NIR-VIS Δr as 0.56°.

In Fig. 7, subtracting Fig. 6(a)'s ADB spectrum from the observed visible-λ rainbow spectra results in a sixfold increase in $\hat{g}$. As in Fig. 2, removing the bluish cloud background spectrum also reddens the intrinsic rainbow: CCTs for this rainbow's mean u', v' decrease from 5515 K to 3934 K. An important caveat is that such spectral corrections are not problem-free: primary rainbow scattering produces the reddest and weakest signal at large r [4], yet all of my intrinsic bows instead steadily grow bluer there (see $r = 43°$ in Fig. 7). This error arises from the fact that the near-zero rainbow scattering at these r cannot be isolated accurately in pixels' visible-λ spectra.

But used with care, Fig. 7 does let us identify the most extreme spectra of its intrinsic rainbow. By avoiding the problematic bluing at its largest r, the primary's bluest and reddest intrinsic colors and spectra can be identified by the bow's maximum and minimum CCTs elsewhere. In Fig. 7, these CCTs occur at $r = 41.55°$ (CCT = 4867 K) and $r = 42.3°$ (CCT = 2904 K), respectively, and each is marked with a black circle. Colorimetrically speaking, these two u', v' result from this particular intrinsic rainbow's most extreme spectra, which makes them worthy of scrutiny.

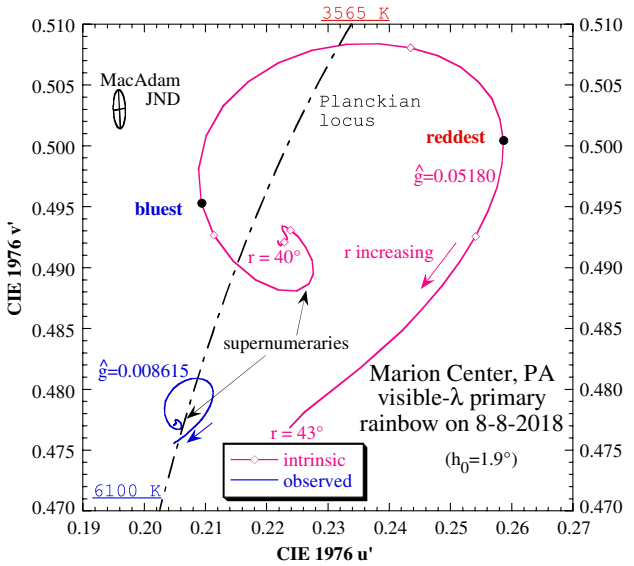

Fig. 7. CIE 1976 UCS diagram with radial chromaticity curves for Fig. 6(a)'s observed and intrinsic natural rainbows at visible λ.

Figure 8 shows these two extreme intrinsic spectra in the VIS and NIR. As is done for the rainbow $u'v'(r)$, these spectra are averaged over a clock angle interval $\Delta\alpha$, which equals 32.1° in Figs. 7 and 8 or a sample size $N \geq 425$ at each rainbow radius. Single-sided error bars that span one standard deviation in L_λ are added to the blue spectrum.

Like many outdoor daytime spectra, those in Fig. 8 are just variations on extraterrestrial sunlight. At Fig. 6's low sun elevation, these variations are quite reddened. They also include the effects of atmospheric absorption bands as manifested by local minima in L_λ, *e.g.*, absorption by oxygen near 690 nm and by water vapor near 720 nm and 815 nm [19]. Figure 7 has special relevance for the natural rainbow because even its bluest color has much energy in the *longwave end* of the visible spectrum

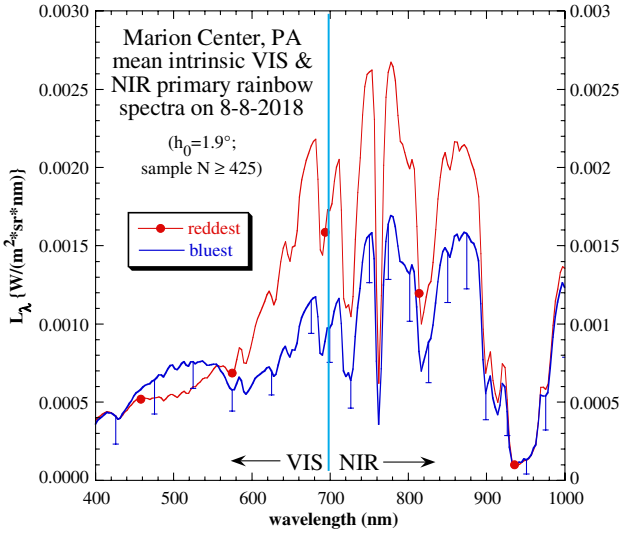

Fig. 8. Visible (VIS) and near-IR (NIR) radiance spectra of direct sunlight convolved with rainbow scattering for the bluest and reddest intrinsic natural rainbow colors seen in Figs. 6 and 7.

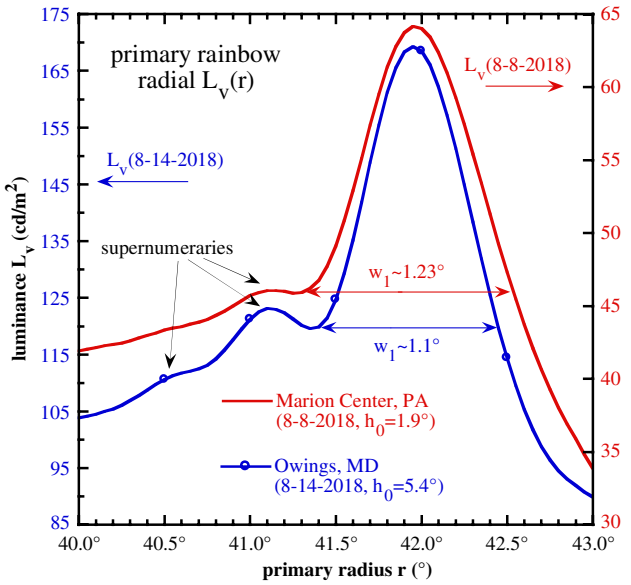

Fig. 9. Radial profiles of luminance $L_v(r)$ for the intrinsic primary bows calculated from Figs. 1(b) and 6(a) (blue line with markers and plain red line, respectively).

(*e.g.*, L_λ integrated from 600–700 nm over any pixel's finite exposure time). Although the resulting color on the inside of Fig. 6's primary is more green than blue, we certainly would not call it reddish even though its spectrum might suggest so.

Instead, this spectrum offers a compelling example of how color constancy and simultaneous color contrast [20] do much to shape our naming of colors. An example of rainbow color constancy is the commonplace that observers persist in assigning the same names to a long-lived rainbow's colors even as its spectra progressively redden with decreasing h_0. Rainbow color contrast occurs whenever a bluish cloud background enhances the perceived yellowness of an adjacent rainbow, even though this enhancement will not appear in the bow's measured $u'v'(r)$ curve.

Natural primary rainbows and their supernumeraries have characteristic photometric as well as colorimetric signatures. Figure 9 shows photometric profiles for the intrinsic rainbows calculated from Figs. 1(b) and 6(a). Two ordinate scales are used in Fig. 9's radial profiles of rainbow luminances $L_v(r)$: the scale on the left is for Fig. 1(b) (*i.e.*, for scan2 on 8-14-2018) whereas that on the right is for Fig. 6(a) on 8-8-2018.

Even though the earlier bow has a 31% smaller $\hat{g}$ and thus is less vivid, its first supernumerary leaves a clear photometric stamp on Fig. 9 at $r = 41.15°$, a feature that is just as clear as its colorimetric hook in Fig. 7. Digital photometry also indicates that the angular widths w_1 of these two primaries [21] are not especially large, with $w_1 < 1.25°$. Yet Fig. 9 also has a very subtle marker for Fig. 1(b)'s second supernumerary, which appears as a $L_v(r)$ inflection point near $r = 40.6°$. This intrinsic rainbow feature is more obvious colorimetrically in Figs. 2 and 3 (see their dashed-line curves) as the right edge of a chromaticity loop near $u' = 0.22$, $v' = 0.49$. Thus even low-contrast rainbow features can be easily revealed via photometry and colorimetry from a natural rainbow's hyperspectral data.

So far, we have analyzed natural rainbows whose colors can charitably be described as modest. That changes in Fig. 10(a) (also identified as scan12), where at the rainbow's base the *observed* $\hat{g} = 0.04894$, or nearly four times larger than the most vivid observed bow examined thus far [see scan2 or Fig. 1(b)]. Slightly purer is Fig. 10(b)'s isolated rainbow fragment, for which the observed $\hat{g} = 0.04993$ was measured at a site ~4 km to the east and several minutes later.

No rain was falling at either location, but archives for the closest weather radar (U.S. National Weather Service site KLWX) indicate that for Fig. 10(a), instantaneous rainfall rates in the rainbow's direction were 0.1–0.45 mm/h, which is equivalent to drizzle or very light rain. By the time that Fig. 10(b) was acquired, this light, showery rain had increased slightly to 0.2–1.5 mm/h. So perhaps surprisingly, heavy rain is *not* required to create bright, vivid primary rainbows, although Fig. 10(b) demonstrates that rainbow $\hat{g}$ can grow when light rain increases.

The observed and intrinsic gamuts for scan12's rainbow are listed both in Table 1 and on Fig. 11. To provide a visual comparison for these gamuts, consider a familiar standard of vivid color: the spectrum projected onto a black background by a sunlit prism. Typical values for such a spectrum's intrinsic gamut are $\hat{g} \sim 0.30$, or ~2.3 times greater than the intrinsic rainbow gamut in Figs. 10(a) and 11. Also in Fig. 11, the ratio $\hat{g}$ (intrinsic)/$\hat{g}$ (observed) ~2.67 for scan12 is much less than the corresponding 4.59 and 6.01 ratios calculated for scan2 [Fig. 1(b)] and Fig. 6(a), respectively.

The smaller intrinsic/observed gamut ratio in Fig. 11 is not surprising, because if a rainbow is bright compared with its background, then color and luminance differences between its observed and intrinsic rainbows will be reduced. Furthermore, Fig. 11 suggests that bright natural rainbows will have observed and intrinsic $u'v'(r)$ curves that are nearly concentric. This too makes sense, because the chromaticity curve for a bright observed rainbow will shift less from its original center when its comparatively weak cloud background is subtracted from the strong rainbow signal.

Fig. 10. RGB images calculated from hyperspectral datacubes acquired for a long-lived (∼1.5 h) natural rainbow on 18 September 2018 at (a) Owings, Maryland at 1803 EDT (scan12; unrefracted $h_0 = 12.2°$) and (b) North Beach, Maryland at 1822 EDT ($h_0 = 8.5°$).

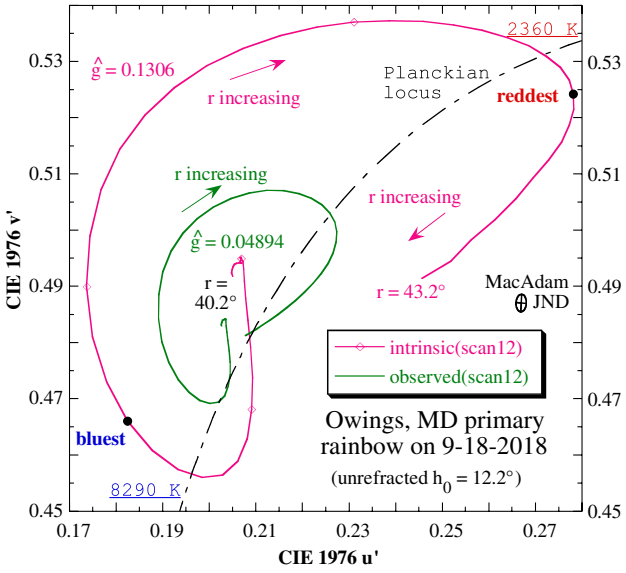

Fig. 11. CIE 1976 UCS diagram with radial chromaticity curves for observed and intrinsic natural rainbows from Fig. 10(a) (*i.e.*, scan12) in drizzle or light rain.

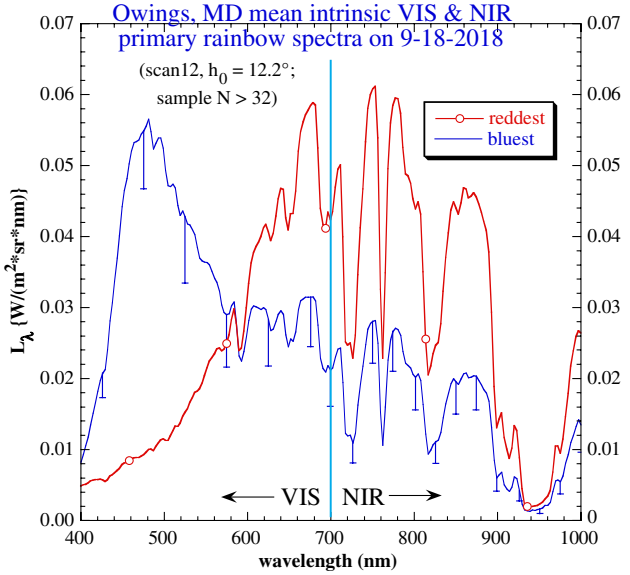

Fig. 12. Visible (VIS) and near-IR (NIR) radiance spectra of direct sunlight convolved with rainbow scattering for the bluest and reddest intrinsic natural rainbow colors from Fig. 10(a) (*i.e.*, scan12).

As in Fig. 7, in Fig. 11 the reddest and bluest $u'v'(r)$ are each marked with a black circle. The corresponding L_λ spectra are plotted in Fig. 12. Unlike Fig. 8's bluest spectrum, Fig. 12's blue counterpart has a pronounced radiance peak at short wavelengths—and a correspondingly distinct blue arc in Fig. 10(a). Spectrally integrated energy at VIS wavelengths now exceeds that in the NIR, unlike the case in Figs. 6 and 8. However, the two red spectra in Figs. 8 and 11 remain quite similar to each other. Thus at very low sun elevations ($h_0 = 1.9°$ in Fig. 6), the intrinsic colors and spectra of most rainbows are dominated at short wavelengths by direct sunlight's reddened spectrum.

Furthermore, the vivid blues seen in Figs. 10(a) and 10(b) disappeared from the 9-18-2018 rainbow by the time its $h_0 = 1.9°$, the same elevation as in Fig. 6's rainbow. By then, Fig. 10's unusually long-lived rainbow consisted of nothing but orange, yellow, and a hint of greenish yellow. So we now have a spectral basis for explaining a venerable rainbow observation: as the sun sets, first blues and then greens disappear from the bow. This is not because shortwave rainbow scattering changes or the cloud background becomes redder (the latter is subtracted in Figs. 11 and 12), but because most shortwave energy has been scattered from direct sunlight before it reaches raindrops that contribute to rainbows seen at low altitudes.

5. CONCLUSIONS

Far from being a closed optical book, the natural rainbow has much left to teach us. Learning its many lessons requires new tools such as the Specim IQ and other field-portable imaging spectrometers, and the wealth of spectrally calibrated radiance data that these can now provide is instructive indeed. First, being able to measure absolute (as opposed to relative) chromaticities permits optically meaningful comparisons of how observed rainbows respond to changes in rainfall rates and spectral changes in sunlight incident on their raindrops (*e.g.*, Figs. 2 and 5). Second, the detailed, highly accurate VIS and NIR rainbow spectra from these spectrometers make possible such invaluable techniques as isolating natural rainbows' intrinsic scattering properties (*i.e.*, the combined spectral effects of sunlight and rainbow scattering functions; see Figs. 3, 4, 7, 8, and 11, 12). Third, hyperspectral imaging of natural rainbows now makes practical and reliable the analysis of even their subtlest photometric and radiometric nuances (*e.g.*, Figs. 8, 9, and 12).

In future rainbow research, additional tools are needed such as solar-disk photometers that are as portable and quick to set up as the Specim IQ. Thus whenever time, topography, and local sunlight conditions permit, we can take the next step of isolating the spectrum of direct sunlight that illuminates nearby rain showers. This will extend the reach of current work on modeling the natural rainbow [4] and will let us analyze the spectra of other often-ephemeral phenomena in atmospheric optics such as ice crystal halos, cloud iridescence, glories, and the green flash.

Funding. National Science Foundation (NSF) (AGS-1664404, AGS-1936028).

Acknowledgments. Raymond Lee's research on natural rainbows has been generously supported by United States National Science Foundation grants AGS–1664404 and AGS–1936028, as well as by the United States Naval Academy's Departments of Mathematics and Oceanography. Opinions, findings, and conclusions or recommendations expressed in this paper are those of the author and do not necessarily reflect the views of the National Science Foundation.

Disclosures. The author declares that no conflicts of interest exist for this paper.

REFERENCES AND NOTES

1. H. R. Condit and F. Grum, "Spectral energy distribution of daylight," J. Opt. Soc. Am. **54**, 937–944 (1964).
2. G. T. Winch, M. C. Boshoff, C. J. Kok, and A. G. du Toit, "Spectroradiometric and colorimetric characteristics of daylight in the southern hemisphere: Pretoria, South Africa," J. Opt. Soc. Am. **56**, 456–464 (1966).
3. J. Hernández-Andrés, J. Romero, and R. L. Lee, Jr., "Colorimetric and spectroradiometric characteristics of narrow-field-of-view clear skylight in Granada, Spain," J. Opt. Soc. Am. A **18**, 412–420 (2001).
4. R. L. Lee, Jr., "Spectral measurement and modeling of natural rainbows," Appl. Opt. **56**, G42–G50 (2017).
5. R. L. Lee, Jr. and D. C. Mollner, "Tropospheric haze and colors of the clear twilight sky," Appl. Opt. **56**, G179–G187 (2017).
6. R. L. Lee, Jr., "What are 'all the colors of the rainbow'?" Appl. Opt. **30**, 3401–3407, 3545 (1991).
7. R. L. Lee, Jr. and A. B. Fraser, *The Rainbow Bridge: Rainbows in Art, Myth, and Science* (Pennsylvania State University, 2001), pp. 238–241, 262–268.
8. S. D. Gedzelman and J. Hernández-Andrés, "Fountain rainbows," Appl. Opt. **47**, H220–H224 (2008).
9. Specim IQ from Specim (Spectral Imaging Ltd.), https://www.specim.fi/iq.
10. For a description of how such RGB images are calculated from visible-wavelength spectra, see R. L. Lee, Jr. and P. Laven, "Visibility of natural tertiary rainbows," Appl. Opt. **50**, F152–F161 (2011).
11. The MacAdam JND is described in G. Wyszecki and W. S. Stiles, *Color Science: Concepts and Methods, Quantitative Data and Formulae*, 2nd ed. (Wiley, 1982), pp. 306–310. MacAdam ellipse semiaxes are not perpendicular in Fig. 2 (and in this paper's other UCS diagrams) because its coordinate axes are scaled anisotropically to show as much colorimetric detail as possible.
12. Although the antisolar point is determined by refracted rather than unrefracted h_0, this paper uses the latter measure because (1) it depends only on time and location and thus requires no detailed profiles of atmospheric constituents and (2) no high-precision data on apparent sun elevation is necessary.
13. Alexander's dark band and other atmospheric optical phenomena are explained on the visually remarkable and scientifically rigorous Atmospheric Optics website, https://www.atoptics.co.uk.
14. J. Hernández-Andrés, R. L. Lee, Jr., and J. Romero, "Calculating correlated color temperatures across the entire gamut of daylight and skylight chromaticities," Appl. Opt. **38**, 5703–5709 (1999).
15. R. L. Lee, Jr., "Twilight and daytime colors of the clear sky," Appl. Opt. **33**, 4629–4638, 4959 (1994). For any u', v' curve, the unnormalized gamut g is a measure of the average distance of its points from the curve's mean u', v'. In turn, $\hat{g} = g/g$ (spectrum locus) so that $\hat{g}$ ranges between 0 for a uniform color and 1 for the spectrum locus.
16. K. F. Palmer and D. Williams, "Optical properties of water in the near infrared," J. Opt. Soc. Am. **64**, 1107–1110 (1974).
17. R. G. Greenler, "Infrared rainbow," Science **173**, 1231–1232 (1971).
18. D. K. Lynch and W. Livingston, *Color and Light in Nature* (Cambridge U. Press, 1995), pp. 106–107.
19. M. Vollmer and J. A. Shaw, "Atmospheric optics in the near infrared," Appl. Opt. **56**, G145–G155 (2017).
20. E. B. Goldstein, *Sensation and Perception* (Wadsworth, 1980), pp. 112–114.
21. The primary width w_1 is defined as $|\Delta r|$ between the radius r of the primary/first supernumerary local minimum in L_v and the larger r where the same rainbow L_v occurs.